NDT&E International 160 (2026) 103665

Contents lists available at ScienceDirect

NDT and E International

journal homepage: www.elsevier.com/locate/ndteint

Automated robotic system for dual ultrasonic and eddy current array integration and data fusion in wire arc additive manufacturing material inspection

Vedran Tunukovic [a,*], Rylan Gomes [a], Shaun McKnight [a], Rastislav Zimermann [a], Euan Foster [a], Charalampos Loukas [a], Randika K.W. Vithanage [a], Ehsan Mohseni [a], S. Gareth Pierce [a], Charles N. MacLeod [a], Stewart Williams [b]

[a] Sensor Enabled Automation, Robotics, and Control Hub (SEARCH), Centre for Ultrasonic Engineering (CUE), Electronic and Electrical Engineering Department, University of Strathclyde, Glasgow, UK
[b] Cranfield University, Welding and Additive Manufacturing Centre, Wharley End, UK

ARTICLE INFO

Keywords:
Data fusion
Dual sensor in-process non-destructive evaluation
Automated phased array ultrasonic testing
Automated eddy current array testing
Wire arc additive manufacturing
Additive manufacturing

ABSTRACT

Wire Arc Additive Manufacturing (WAAM) is a direct energy deposition method that enables the fabrication of large, complex metal components with minimal material waste, making it a key technology within Industry 4.0. However, WAAM is prone to weld-like defects, such as lack of fusion, keyholes, and porosities, which compromise structural integrity and require a reliable Non-Destructive Evaluation (NDE). Conventional post-process inspection methods, including Ultrasonic Testing (UT) and X-ray imaging, can detect such defects but often lead to costly rework once fabrication is complete. This work presents a dual-sensor robotic inspection system enabling simultaneous phased array UT and Eddy Current Testing (ECT) during WAAM deposition for early defect detection and efficient process monitoring. The system integrates an industrial manipulator with closed-loop force-torque control for repeatable layer-wise scanning without tool changes or process interruption. The system was evaluated using two Ti-6Al-4V reference blocks that replicated WAAM geometries and contained artificial defects. A depth-weighted C-scan data fusion approach, supported by targeted ECT denoising, improved contrast-to-noise ratio by 4.44 dB and 9.02 dB for the two samples, respectively. The approach was further validated on a titanium WAAM sample containing embedded tungsten inclusions, demonstrating the robustness of the methodology. A receiver operating characteristic analysis further confirmed the improved defect discrimination of the fused data, consistently resulting in higher area-under-curve values than either UT or ECT alone across all evaluated samples.

1. Introduction

Additive Manufacturing (AM) is a process that leverages precise layer-by-layer material deposition based on a Computer-Aided Design (CAD) model and bespoke deposition planning software. In contrast to conventional subtractive manufacturing methods like machining or grinding, AM allows for rapid prototyping while significantly minimising material wastage. The market value of AM increased considerably, from evaluations of €3.7 billion in 2015 [1] to approximately €37.93 billion in 2024, with projections reaching around €46.71 billion in 2025 [2]. This substantial growth underscores its pivotal role in shaping the trajectory of Industry 4.0 [3], with the adoption of AM technologies driving this shift, especially in the field of aerospace and civil engineering [4].

Among many AM methods, Wire Arc Additive Manufacturing (WAAM) stands out as a direct energy deposition method suitable for the fabrication of complex geometry components, offering high deposition rates and the potential for manufacturing large-scale components [5]. This method has proven suitable for materials such as steel, nickel-based alloys, and titanium. While WAAM optimises material usage, certain challenges have been recognised. Specifically, the presence of weld-like defects, such as lack of fusion, key holes, and porosities, poses a risk to both the serviceability and mechanical integrity of the manufactured components. Consequently, conducting thorough material inspections is

* Corresponding author.
E-mail address: vedran.tunukovic@strath.ac.uk (V. Tunukovic).

https://doi.org/10.1016/j.ndteint.2026.103665
Received 4 November 2025; Received in revised form 10 January 2026; Accepted 1 February 2026
Available online 10 February 2026
0963-8695/© 2026 The Authors. Published by Elsevier Ltd. This is an open access article under the CC BY license (http://creativecommons.org/licenses/by/4.0/).

essential to identify potential material shortcomings and avoid critical failures. Non-Destructive Evaluation (NDE) is an umbrella term for techniques employed to inspect materials without altering their properties or functionality. NDE encompasses a wide range of methods, including visual inspection, thermographic imaging, radiographic testing, Ultrasonic Testing (UT), and Eddy Current Testing (ECT). In the context of AM, the most commonly used NDE methods are X-rays, UT and ECT [6,7].

The layered structure of WAAM provides the opportunity for the application of inter-layer inspection, offering advantages over conventional post-manufacturing inspection. By detecting defects immediately after deposition, this approach reduces material waste, deposition energy, and time, while minimising the need for extensive rework and preventing the defect from remaining in the final product or propagating through subsequent layers. However, the implementation of in-process inspections presents a new set of challenges. The elevated temperature of freshly deposited material presents a limitation for most NDE equipment and sensors. Additionally, the time between deposition of layers (dwell time) is a critical parameter of WAAM, directly impacting the microstructure and the quality of the manufactured components by influencing thermal gradients, residual stresses, and interlayer fusion [8]. Therefore, in-process inspection must be performed rapidly within the available dwell time to enable the timely deposition of subsequent material layers. Lastly, due to the complex surface geometry and potential defect locations, the manufactured part is oftentimes scanned with several NDE modalities. This is due to the inherent shortcomings of individual NDE methods, which are not capable of confidently capturing all relevant information.

Ultrasonic testing is a versatile NDE method that commonly leverages the piezoelectric effect, one of several mechanisms for generating ultrasonic waves. In this process, the voltage applied to the ultrasonic transducer is converted to mechanical energy, generating acoustic waves with frequencies exceeding 20 kHz. These ultrasonic waves propagate through the material, interacting with its structure and features, thereby inducing scattering and reflection. By recording these reflections, it is possible to infer valuable information about the internal structure of the inspected material. Phased Array Ultrasonic Testing (PAUT) is a subcategory of UT that focuses on the use of ultrasonic arrays, where a group of individually controlled small ultrasonic transducers enable advanced electronic scanning modes such as beam scanning, focusing and steering. The array technology also supports raw full data acquisition, known as full matrix capture, for post-acquisition advanced imaging [9–11]. The data captured with PAUT is most often displayed as a B-scan (a two-dimensional cross-sectional view) or a C-scan (a planar top-down view mapping the volumetric signal amplitude or time-of-flight across the surface), with each format offering a distinct perspective of the scan data and the subject material. However, UT's detection sensitivity is limited to half of the size of the wavelength, making it impossible to detect defects smaller than this threshold. Moreover, the uneven quality of the WAAM surface and the presence of an ultrasonic “dead zone” pose challenges in identifying features close to the source of the ultrasonic pulse [12]. The latter can often be rectified by using stand-off wedges/materials to remove the dead zone from the test piece.

Eddy current testing employs electromagnetic principles where a multi-turn coil is excited using alternating voltage, establishing a primary alternating magnetic field encircling the coil. When positioned in proximity to a conductive material, the coil induces a voltage in the conductor, generating eddy current flow, which generates its own magnetic field opposing the primary field directly. Variations in material conductivity, magnetic permeability, and discontinuities affect the eddy currents' intensity and uniformity, resulting in changes to the secondary magnetic field. Consequently, this induces a complex impedance shift in the pick-up coil. ECT is widely used for rapid inspection of metal conductors for surface and subsurface flaws [13]. Although ECT is favoured for non-contact rapid testing, the exponential decay of the eddy current density as a function of inspection depth decreases the possibility of detecting deeper volumetric defects. The study detailed in Ref. [14] evaluated the detectability of ECT of sub-surface defects within an additively manufactured cobalt-based alloy specimen. It was reported that defects of size 0.5 mm or more were detected at a depth of 0.5 mm, measured from the surface. Studies [4] and [15] investigated the feasibility of using ECT for inline inspection of titanium and cobalt-based AM components. The results demonstrated excellent sensitivity to artificially embedded defects up to 4.5 mm deep from the surface.

The integration of industrial manipulators has significantly advanced the automation in NDE, leading to improved scanning speeds and efficiency compared to manual techniques. This transformation has resulted in increased precision and repeatability of sensor delivery while reducing labour requirements and the potential for human error [16]. Consequently, there is a growing academic interest and research focus on enhancing robotic controls and automating various NDE workflows [16–19]. These works are key enablers in the paradigm shift towards Industry 4.0, allowing for the integration of modern technologies and upgrading currently established workflows from post-process to in-process methods.

Several research groups tackled the automation of NDE for WAAM. The study detailed in Ref. [20] demonstrated the potential for combining arc-based AM with automated NDE through a collaborative robotic mechanism. The development of multi-robot cells, driven by a sensor-enabled robotic system and a real-time embedded controller, has achieved full automation, enabling real-time communication, data acquisition, and precise control of the manufacturing and inspection processes simultaneously. Similarly, the authors in their earlier publications [21–23] demonstrated fully automated continuous monitoring of multi-pass welding through robotic NDE. The adaptive pose control during the scan of NDE sensors on complex geometry components was accomplished through state-of-the-art robot kinematics software, operating in real-time intervals on the KUKA Robot Controller [18]. The elevated temperature in WAAM and welded components was tackled with a newly developed high-temperature resistant PAUT roller probe and active cooling system, featuring a soft heat-resistant polymer tyre, which proved efficient in dry-coupled inspection of test components at sustained elevated temperatures, surpassing 300 °C [24]. Additionally, it was shown that the probe's soft tyre can adapt to irregular, un-machined surface profiles of a WAAM component [25]. Nevertheless, establishing a dry-coupled contact of the PAUT roller probe on a rough undulated surface, like those of freshly deposited WAAM, might cause insufficient coupling at places which give rise to an extended dead zone beneath the inspection surface (*i.e.*, near-surface reverberations caused by the poor surface coupling). Therefore, flexible conformable ECT arrays, with higher sensitivity to surface and near-surface defects, could be deployed to complement the PAUT volumetric inspections and increase the reliability. In this regard, a recent study highlighted the effectiveness of combining the PAUT with ECT to comprehensively assess the volume of WAAM components [4].

Data fusion in NDE is a method of combining data captured from different sensing modalities to provide a more comprehensive assessment of the inspected material. This integration leverages the strengths of each method while compensating for its limitations. Over the past two decades, there has been a growing interest in data fusion techniques in NDE, with a substantial body of work [26–29]. However, limited research has been dedicated specifically to fusing UT and ECT data. In Ref. [30], the authors explored the fusion of UT amplitude and ECT C-scans using machine learning approaches, including pixel-level fusion, feature-level fusion, and symbol-level fusion. Similarly, the work detailed in Ref. [31] focused on the use of machine learning with radial basis function networks to merge scans performed on aluminium samples. Authors in Ref. [32] utilised a complex image fusion method based on traditional image processing techniques. In Ref. [33], researchers worked on data fusion of pulsed ECT and UT for stress measurement

testing in aluminium samples. This was achieved by extracting relevant signal features from both NDE modalities and applying fuzzy logic, achieving improvements in the accuracy and reliability of conducted measurements. In the continuation of the previous work [34], the authors have employed artificial neural networks for data fusion, further improving the results. A dual-probe setup was proposed in Ref. [35], where a combination of an electromagnetic acoustic transducer for the production of surface acoustic waves was combined with a pulsed eddy current probe. In this work, data fusion was achieved with thresholding and weighted logic, depending on the type of inspected material. A similar setup was introduced in Ref. [36], with authors reporting achievement of great results on both ferromagnetic and non-ferromagnetic materials. While these studies demonstrate the feasibility of UT-ECT data fusion on aluminium and steel samples of simple geometry, several important gaps remain:

- None of the prior studies address fusion on titanium WAAM components, which feature complex surface geometries.
- In-process inspection during additive manufacturing typically relies on separate scans when multiple modalities are used.
- An integrated workflow combining synchronised dual-sensor inspection using PAUT and ECT arrays with a data fusion approach has not been demonstrated.

Building on previous work [20], focused on the development of a high-temperature roller probe designed for in-process inspection of Ti-6Al-4V WAAM, this study explores the applicability of dual-sensor deployment and data fusion on reference Ti-6Al-4V samples, machined to replicate the complex surface profiles typically observed in WAAM components. The study also demonstrates the data fusion of the two NDE data streams captured during the live deposition of a WAAM Ti-6Al-4V with embedded tungsten inserts to mimic process defects such as lack of fusion and inclusions, to serve as a proof of concept before translation to live deposition. Novelty and key contributions of this work include:

- **Design and development of a bespoke dual probe assembly**: The assembly accommodates both a high-temperature dry-coupled PAUT roller probe and a high-temperature ECT flexible padded array. This design enables simultaneous scanning of both modalities and maintains a consistent spatial relationship between sensors without the need for separate scans or recalibration. Moreover, the dual probe assembly negates the requirement for separate robot manipulator's load calibrations for the contact force when inspecting with individual modalities.
- **Data fusion of UT and ECT data**: A method was developed that combines UT and ECT data using the depth-weighting fusion approach, in which ECT primarily contributes to surface and near-subsurface detection (within the skin depth), while UT provides sensitivity to deeper regions of the volumetric scan. Furthermore, ECT data were processed through phase rotation and median subtraction per channel, reducing acquisition noise and closely aligning recorded defect amplitude levels between the modalities.
- **Case study on WAAM titanium samples**: The proposed methods are tested on two Ti-6Al-4V reference block samples, and on a sample manufactured via WAAM. These reference samples were characterised by complex surfaces and a range of manufactured defects to scrutinise the detection capabilities of both inspection modalities. The fusion approach is then showcased on a WAAM sample with embedded inclusions and UT/ECT data streams captured in process. The study also demonstrates a closed-loop automation system for deployment and data acquisition developed in the LabVIEW environment.

The rest of this paper is organised as follows: Section 2 defines the used materials and methods, results and discussion are presented in Section 3, and the conclusion with prospective future work is detailed in Section 4.

2. Materials and methods

2.1. Overview

This study focuses on a dual-sensor assembly designed to house PAUT and ECT sensors, integrated with an industrial manipulator for inspecting: 1) two titanium reference block samples that replicate the geometry of WAAM components, and data fusion approaches to simplify the data analysis, 2) a WAAM deposited Ti-6Al-4V component, for which the PAUT/ECT data was captured in process and in between the layers to demonstrate the benefits and industrial pertinence of the data fusion approach established on reference samples in the first stage.

To assess the performance of each sensing modality, the reference blocks were fabricated with various artificial defects to partially simulate acoustic responses from flaws that may occur in WAAM components. These samples provide a controlled, less complex inspection scenario, serving as a proof of concept before deploying these techniques in in-process inspections. The following sections detail the individual components of the experimental setup.

2.2. Additive manufacturing samples

For this study, two reference samples with a surface profile similar to titanium WAAM were created to evaluate the dual sensor deployment feasibility and the following data fusion algorithms. Sample A was made from Ti-6Al-4V with dimensions of 500.0 x 30.0 × 30.0 mm. To scrutinise the NDE modalities' detection capabilities and their complementarity in detection, the sample included four Back Drilled Holes (BDH) with 3.0 mm diameter positioned at depths of 2.0, 4.0, 6.0, and 8.0 mm from the surface of the material. In addition, four Side Drilled Holes (SDH) of the same diameter were manufactured at depths of 3.5, 5.5, 7.5 and 9.5 mm. Lastly, six stepped notches were drilled into the back of the sample at depths starting at 2.0 mm and ending at 12.0 mm with increments of 2.0 mm (all depth measures are from the surface). The surface of this sample was smooth, with a curved profile with a 5 mm fillet radius to mimic the side profile of components manufactured via the WAAM process.

Sample B was created similarly, using the same material and dimensions as Sample A. However, manufactured defects in this sample included six SDHs with a 2.0 mm diameter, positioned at depths starting at 1.0 mm and increasing in depth with increments of 1.0 mm. Additionally, twelve BDHs with a 1.0 mm diameter were created, with six positioned at the centre of the material and six placed with a 15.0 mm offset from the centre of the sample. These were positioned at similar depths, starting at 1.0 mm with increments of 1.0 mm. The major difference was the geometry and surface finish, as Sample B had a rough surface achieved through computer numerical control machining. This change mimics the surface of real WAAM samples and acts as a scatterer of ultrasound, therefore making the inspection more challenging. CAD files of both reference samples are illustrated in Fig. 1.

To demonstrate the effectiveness of the approach, the methodology was tested on an additional sample C, which measured 300.0 × 25.0 × 25.0 mm and was manufactured from the same material as the previous samples, in an automated robotic WAAM cell, as detailed in Ref. [4]. Deposition followed an oscillating pattern with a current of 150 A, a wire-feed speed of 2.5 m/min, and a robotic velocity of 0.005 m/s. Tungsten tubes (30.0 mm in length, with internal and external diameters of 1.0 mm and 3.0 mm, respectively) were embedded into pockets created by a grinding machine in the third deposited layer. Two tubes were embedded within the sample, one oriented longitudinally and the other transversely relative to the sample length, after the completion of layer 3. Tungsten balls of 1.0 mm, 2.0 mm, and 3.0 mm diameter were subsequently embedded after layer 4. ECT scans of Sample C were

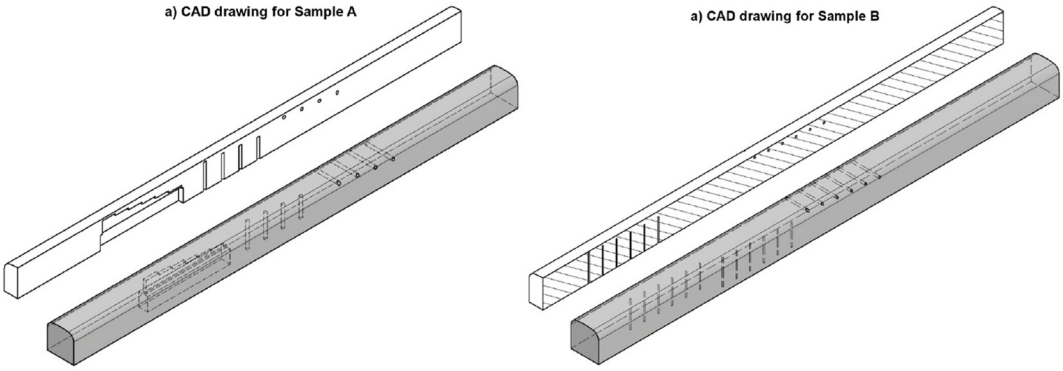


Fig. 1. a) CAD model of Sample A; and b) CAD model of Sample B.

conducted at two build stages: after layer 4 (before embedding the tungsten balls, with only the tubes present) and after layer 5 (following the inclusion of the tungsten balls). The ECT image used for data fusion was generated as a combined representation of these two layers, retaining information of embedded features from both layers. A model of the inspected sample is shown in Fig. 2.

2.3. Robotic setup

The sensing equipment was delivered using the 6-axis industrial manipulator KUKA KR90 R3100 Extra HA [37]. Used industrial manipulator ensured precise and accurate sensor delivery, with a pose repeatability of ± 0.06 mm, and a maximum reach of 3095 mm. A LabVIEW Virtual Instrument environment on a desktop personal computer was employed to define robotic path planning for horizontal movement and to acquire data from both ECT and PAUT modalities.

The vertical inspection tool pose was controlled using the Schunk GmbH & Co. FTN-GAMMA-IP65 SI-130-10 Force Torque (FT) sensor [38]. Positioned between the manipulator arm and the UT roller probe, the FT sensor was used to control contact force between the probe and the material surface during inspection. The control system was configured to maintain a nominal contact force of 70 N, which was experimentally determined to provide adequate acoustic coupling quality for the roller probe used in this study. To protect the sensing equipment, a maximum force threshold of 130 N was implemented as a fail-safe condition. If the measured vertical force exceeded this value, the scanning operation is immediately terminated, and a stop sequence is triggered. This threshold accounts for force fluctuations due to the scan speed, local surface geometry variations, and limitations in the force control response of the proposed system. For stable scanning, the horizontal movement velocity of 10 mm/s was employed. The crucial advantage enabled by the robotic setup is the automatic encoding of the captured data, enabling easier data registration and alignment in later steps.

2.4. Ultrasonic testing setup

In inter-layer in-process inspection of WAAM, elevated post-deposition material temperatures complicate the PAUT inspection deployment in several ways. In conventional PAUT, a thin layer of gel or water is typically applied to the material surface to eliminate air pockets and facilitate the propagation of ultrasonic waves into the material. However, the use of coupling should be avoided in WAAM, as this can introduce contamination into the deposition process. Furthermore, higher inspection temperatures limit the choice of equipment, as commercially available roller probe tyre materials are often unsuitable for high-temperature environments.

To address these challenges, an in-house designed and manufactured PAUT roller probe was developed. Its tyre material is selected from a range of soft, high-temperature resistant silicone polymers to conform to the surface and drive out the air pockets without the need for liquid coupling. Although this solution unlocks in-process inspection capability, the absence of liquid coupling increases the acoustic impedance mismatch between the tyre and the component, reducing energy

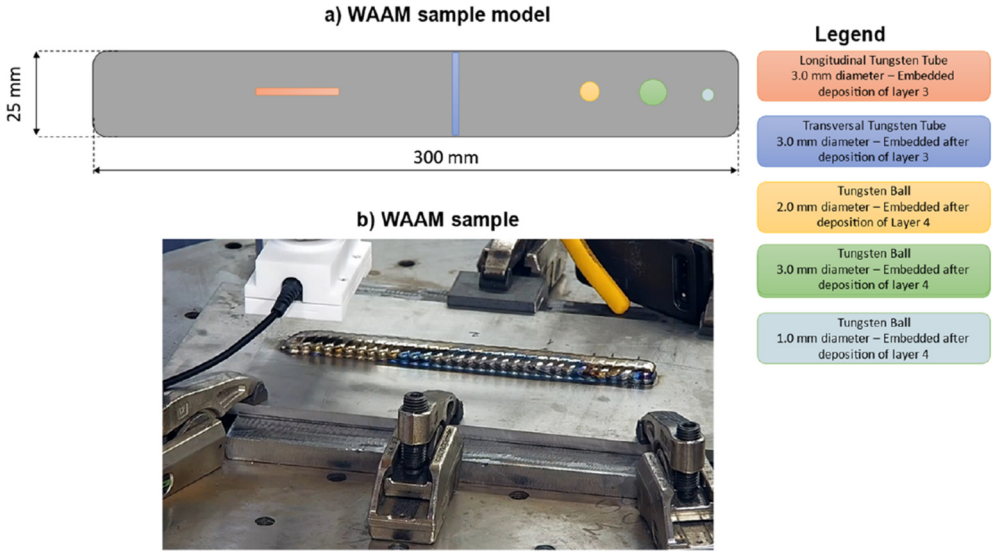


Fig. 2. a) A model of the Sample C (WAAM sample) and b) The inspected WAAM sample.

transmission and lowering signal-to-noise-ratio (SNR). To this end, UT was conducted using the custom-built in-house PAUT roller probe, specifically designed for high-temperature operation based on previous work detailed in Ref. [20]. This roller probe contains a 0° wedge, serving as a delay line between the array and the tyre interface. The used PAUT array has 64 individual ultrasonic transducers operating at a central frequency of 5 MHz, with an elevation of 10 mm, and an element pitch of 0.5 mm.

The array was controlled using a Peak NDT Ltd MicroPulse 6 unit [39], allowing for the design of delay laws for 128 transmission/reception channels. A linear electronic scan with a sub-aperture of 32 elements was used, driven with a voltage of 200 V. As linear unfocused scanning resulted in poor SNR and noisy scans, the UT scanning was set up to focus on a depth of 8.0 mm from the sample surface. Data was recorded at a sampling rate of 100 MHz, with a gain of 50 dB, accompanied by a pulse repetition frequency of 760 Hz. The combination of high voltage, high gain, and a large sub-aperture was used to enhance energy transmission into the sample due to the dry coupling operation. The illustration of the PAUT roller probe assembly is presented in Fig. 3.

2.5. Eddy Current Testing setup

A commercial 32-element padded ECT array with a centre frequency of 50 kHz and an operating frequency range of 15-250 kHz was used to perform the ECT scans. A total of 32 pancake coils within the probe were arranged in 2 rows of 16 coils, and controlled with a 64-element Eddyfi Ectane 2 controller [40]. During the inspection, the data acquisition was set to 200 Hz, while the data was acquired with 40 dB of gain, 50 kHz operating frequency, and a voltage excitation of 10 V. The array probe has the capability of collecting impedance data in two different orientations (axial and transversal) corresponding to different transmit and receive pairs. In this study, the axial impedance was used as the defect response was observed with better resolution compared to the transversal impedance. The padded surface of the probe allowed better conformity to the wavy WAAM surface, reducing the effects of lift-off and tilt variations. Fig. 4 presents a schematic view of the inspected sample and UT and ECT sensors.

2.6. Assembly for ultrasonic and eddy current equipment

An assembly for the simultaneous delivery of PAUT and ECT sensors was designed for this study. The assembly enabled the attachment of two sensors, with the PAUT roller probe positioned in the front, followed by a spring-loaded bracket for the ECT sensor. This arrangement offered three significant advantages:

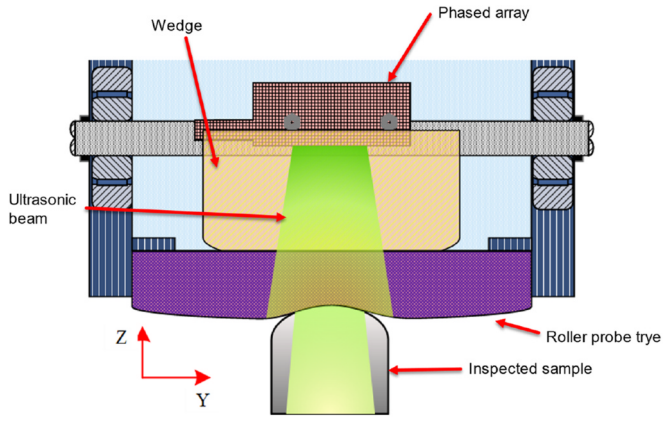


Fig. 3. Illustration of the phased array ultrasonic testing roller probe assembly with an ultrasonic beam propagating into the sample. Scanning is conducted along the X-axis, which is oriented perpendicular to the image plane.

1. Establishing a known offset between the sensors minimises the need for extensive data processing to align the two modalities.
2. Improving the safety of ECT probe deployment by allowing the PAUT probe to establish initial contact with the sample.
3. Reducing inspection time by applying both sensors simultaneously, rather than the sequential and individual deployment used in traditional NDE for WAAM inspection.

Since controlling and establishing a consistent contact force for the PAUT roller probe to the sample is critical, the PAUT roller probe was placed in the lead position directly beneath the FT sensor, while the EC sensor is mounted on a spring-loaded translation stage to actuate the height of the probe independently. This setup ensured that the roller probe achieved the predetermined contact force of 70N, as controlled in the LabVIEW environment. Meanwhile, the spring-loaded brackets allowed for fine adjustments, ensuring precise positioning and adherence of the ECT probe at much lower contact force of 30N. Both the CAD model and the final prototype of the assembly are shown in Fig. 5, while Fig. 6 depicts a block diagram of the full experimental setup.

2.7. Signal processing

The integration of PAUT with the robotic system and performing scans on the component allowed to capture a complete 3D volume of the material, stored in [Array element (x), Time-of-flight (t), Scan position (y)] format. Before the visualisation of ultrasonic data, signal gating and Hilbert transform were performed at the A-scan level. These established signal processing procedures are widely used in industrial settings, allowing for easier interpretation of collected UT data and the successful creation of ultrasonic C-scans, a 2D top-down view of the inspected sample [41,42]. Considering that the width of the inspected sample was smaller than the active aperture of the PAUT array, the A-scan data associated with the elements located at the extremity of the array was removed to truncate the scan width, as these elements don't contribute to the beam that reaches the sample's interior, ensuring only the relevant sections related to the inspected sample were retained for further analysis and interpretation.

The visualisation of ECT data involved processing rectified impedance versus scan position readings for axial channels. The data from all channels was phase-rotated with a fixed phase angle to maximise the defects' SNR ratio. Normalisation of both ECT and UT data was implemented relative to the maximum amplitude in both C-scans, constraining the amplitude values between 0 and 1. This process is straightforward for the UT scans, as maximum recorded amplitude was observed in the front wall of the sample; however, for an ECT scan, a known defect or feature is needed to do this successfully. Therefore, ECT scans were normalised to the maximum defective responses corresponding to defects located closest to the top surface of the material.

2.8. Data fusion

The data fusion method is motivated by the physical properties of both modalities. UT encounters challenges when:

- Attempting to identify potential defects situated near prominent geometrical features, such as the front wall of the sample. These features generate strong acoustic responses, overshadowing smaller defective indications.
- Dealing with a complex and uneven sample surface, which scatters the ultrasonic beam, reducing the SNR and complicating signal interpretation.
- Being unable to leverage coupling to enhance energy transmission due to elevated material temperatures.
- Operating with a rigid array and wedge, making perfect adherence to the inspection surface impossible. This is further complicated by the limited field of view of the ultrasound, determined by the small

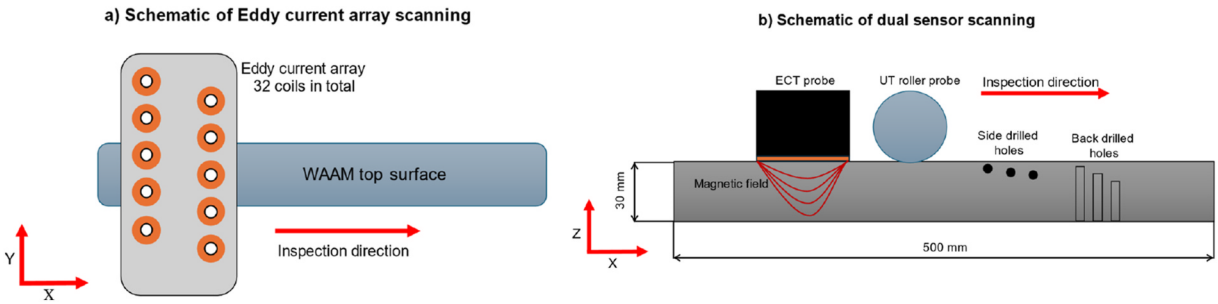


Fig. 4. a) Schematic of eddy current scanning; and b) Schematic showing how the eddy current probe is positioned behind the ultrasonic roller probe in dual sensor inspection.

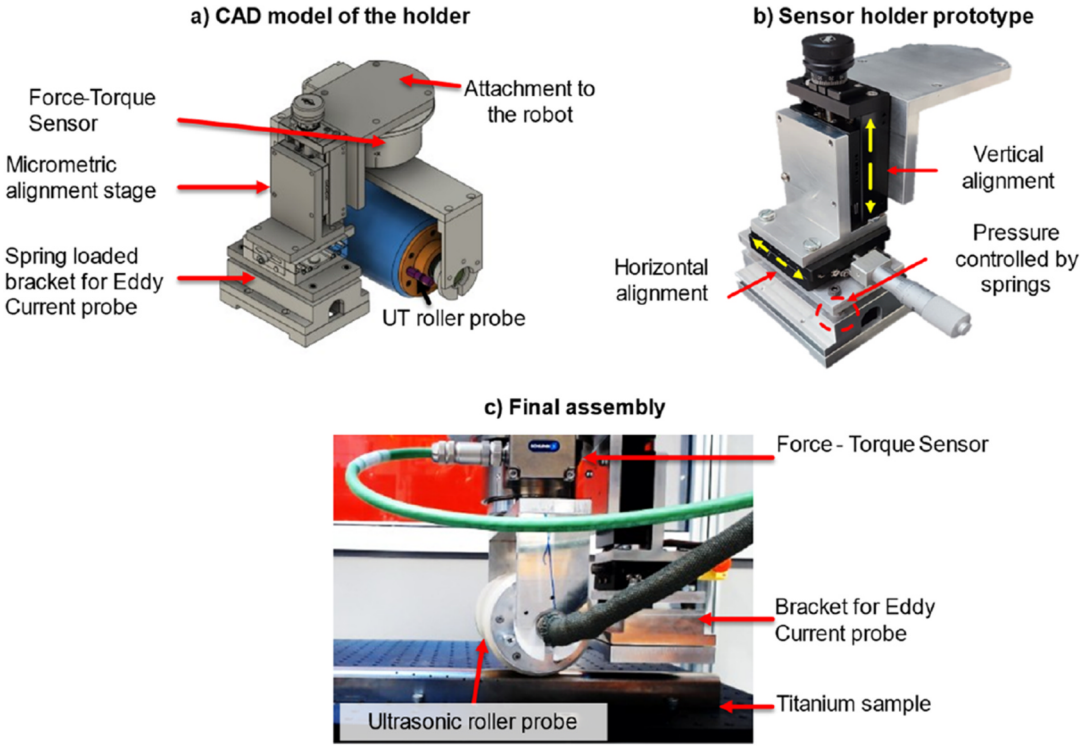


Fig. 5. a) CAD model of the dual sensor assembly; b) the sensor holder prototype; and c) the final dual sensor assembly.

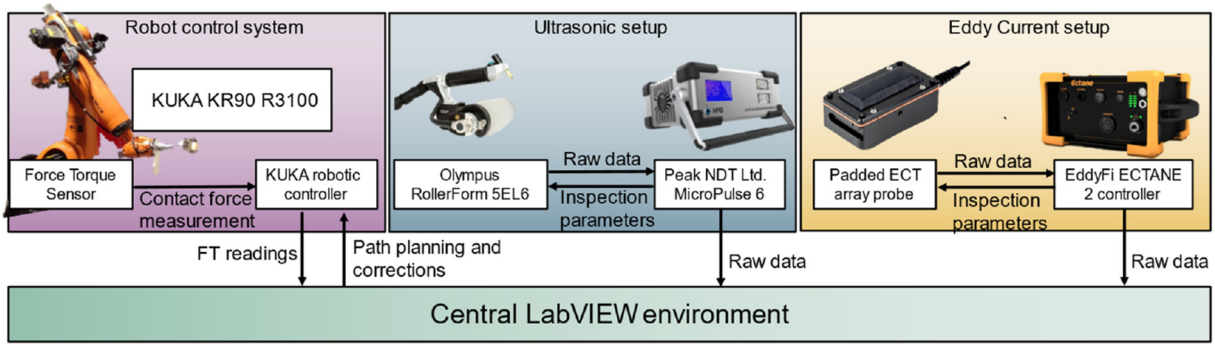


Fig. 6. Block diagram of the experimental setup.

contact window area between the wedge and the inspection surface. As a result, blind spots at the corners beneath the surface are unavoidable.

On the other hand, ECT excels at imaging surface and subsurface defects if they are within the skin depth. The effective ECT skin depth (3δ) represents the depth where the eddy current density reduces to about 5% of the density on the surface; this depth can be described with Eq. (1):

$$\delta = \frac{1}{\sqrt{\pi f \mu \sigma}} \quad \text{Eq. 1}$$

where δ represents skin depth, f is the used coil frequency, μ is the magnetic permeability, and σ is the electrical conductivity of the inspected material. As μ and σ are material properties, the excitation frequency directly dictates the skin depth. For the inspected Ti-6Al-4V material, μ of 1.25×10^{-6} H/m, σ of 5.62×10^{5} S/m, and f of 50000 Hz result in a skin depth of ~3.0 mm.

Considering the bulk inspection coverage of PAUT and the superior near-surface performance of ECT, fusing the data on a pixel level between the ECT and PAUT data is deemed promising. The format of captured data is as follows:

- **ECT Data**: A 2D intensity array/image with dimensions [Array channel (x), Scan position (y)], where each channel corresponds to an impedance amplitude, and the scanning step represents the position along the scanning path.
- **UT Data**: A 3D array with dimensions [Array element (x), Time-of-flight (t), Scan position (y)], where each A-scan captures an individual ultrasonic signal, the time series corresponds to the signal over time, and the scanning step represents the position along the scanning path.

However, since ECT data is in 2D and PAUT data is in 3D, amplitude C-scans of the PAUT data are created to reduce the dimensionality of UT data to match ECT. The amplitude C-scan presents a top-down view of the inspected sample, displaying the maximum amplitudes. Signal time gating is crucial for the generation of UT C-scans; strong front wall indications need to be removed to prevent them from masking the ultrasonic indications of lower amplitudes within the internal portion of the material.

Let PAUT data be represented as a 3D array $U(x,t,y)$, where x is the array element (A-scan index), t is the time-of-flight sample, and y is the scanning step along the inspection path. The ECT data are presented as a two-dimensional C-scan image $C_{ECT}(x,y)$, where x corresponds to the ECT array channel and y to the scanning step. A gated amplitude C-scan $C_{UT}(x, y)$ is calculated as:

$$C_{UT}(x,y) = \max_{t \in [t_1, t_2]} |U(x,t,y)| \quad \text{Eq. 2}$$

Where $[t_1,t_2]$ defines the time gate excluding the front-wall response and extending up to the back-wall reflection. This operation reduces the PAUT data dimensionality to match the 2D ECT representation. Normalisation of both modalities is expressed as:

$$C_{UT}^{norm}(x,y) = \frac{C_{UT}(x,y)}{max(C_{UT})}, C_{ECT}^{norm}(x,y) = \frac{C_{ECT}(x,y)}{max(C_{ECT})} \quad \text{Eq. 3}$$

Where the superscript norm denotes normalised amplitude values scaled to [0,1].

Since ECT provides high sensitivity to surface and near-surface defects within the skin depth, while PAUT provides volumetric coverage, the two normalised C-scans contain complementary information. Given that both datasets are spatially correlated and normalised to a common scale, a pixel-level additive fusion is used to preserve indications from both modalities without introducing additional model assumptions. The fused image is defined as:

$$F(x,y) = \frac{C_{UT}^{norm}(x,y) + C_{ECT}^{norm}(x,y)}{max\left(C_{UT}^{norm}(x,y) + C_{ECT}^{norm}(x,y)\right)} \quad \text{Eq. 4}$$

This data fusion logic is illustrated in Fig. 7. The resulting data fusion dataset contains both ECT and UT data, leveraging their respective strengths in the areas of the scan where they excel.

2.9. Receiver operating characteristic

To quantitatively evaluate the performance of the data fusion approach, a Receiver Operating Characteristic (ROC) analysis was performed. ROC curves represent a trade-off between sensitivity and specificity for binary classification methods. In the context of NDE C-scans, pixels or regions identified as defects are considered positive, while defect-free pixels are negative. For each pixel in the UT, ECT, and fused C-scans, a binary classification is performed by applying a threshold T to the normalised amplitude values $C^{norm}(x,y)$:

$$Detected(x,y;T) = \begin{cases} 1, C^{norm}(x,y) \geq T \\ 0, C^{norm}(x,y) < T \end{cases} \quad \text{Eq.5}$$

Using the manually extracted defective and pristine areas as ground truth, the following metrics are computed at each threshold T:

$$True\ Positive\ Rate\ (TPR) = \frac{Number\ of\ correctly\ detected\ defect\ pixels}{Total\ number\ of\ defect\ pixels} \quad \text{Eq.6}$$

$$False\ Positive\ Rate\ (FPR) = \frac{Number\ of\ defect-free\ pixels\ incorrectly\ detected\ as\ defects}{Total\ number\ of\ defect-free\ pixels} \quad \text{Eq.7}$$

The ROC curve is then obtained by plotting TPR vs FPR for a range of thresholds. Lastly, the Area Under the Curve (AUC) is also computed to provide a single quantitative measure of the overall detection performance:

$$ROC_{curve} = \{(FPR_1, TPR_1), (FPR_2, TPR_2), \ldots, (FPR_n, TPR_n)\} \quad \text{Eq.8}$$

2.10. Contrast to noise ratio calculation

To quantify the effect of pixel-wise data fusion, the Contrast-to-Noise

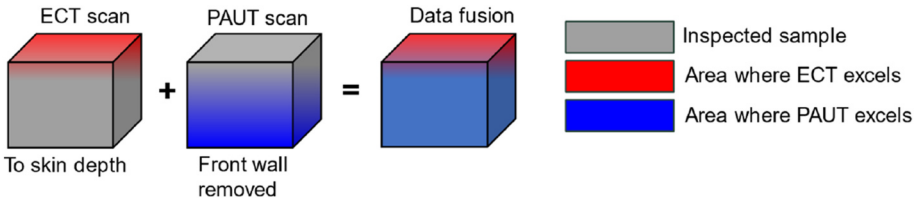


Fig. 7. Illustration of the data fusion logic of UT and ECT data.

Ratio (CNR) is calculated. CNR was introduced in 1983 [43] and is an image quality metric that builds upon the basic contrast formulation, which compares the mean signal value to the mean noise (background) values. By incorporating the standard deviations of both signal and noise in the calculation, CNR offers a more accurate measure of a feature's detectability against the background of the image. CNR is widely used in the medical field to determine the visibility of lesions in medical scans such as magnetic resonance imaging and radiography. To ensure accuracy and repeatability, the CNR was evaluated on signal amplitudes captured from manually extracted defective and pristine areas in UT, ECT, and fused data, respectively. In an ideal scenario, the pristine areas of the scan, representing the background of the image, would be extracted from a reference scan where no defects are present. However, in the present study, access to such defect-free AM samples was limited, making it necessary to work with the manually extracted sections of the available data. CNR is calculated with Eq. (9):

$$CNR\ (dB) = 20\log_{10}\left(\frac{abs\left(\mu_d - \mu_p\right)}{\sqrt{\sigma_d^2 + \sigma_p^2}}\right) \quad \text{Eq. 9}$$

Where μ_d and μ_p represent the mean amplitude values of the defective and pristine (background) areas, respectively, and σ_d and σ_p represent the corresponding standard deviations in the defective and pristine areas of the scans. The resulting ratio is then converted to a decibel (dB) scale for easier interpretation of the results. CNR values can be positive or negative, with higher positive values indicating better contrast between defects and the scan background, making defects easier to identify. In contrast, low or negative CNR values suggest poor contrast, making it difficult to distinguish defective areas from the background.

3. Results and discussion

3.1. Results sample A

Visual inspection of the PAUT scan for sample A (Fig. 8a) reveals all notches clearly, but only 3 out of 4 SDHs are visible, with the last BDH barely identifiable. This observation is consistent with the calculated CNR values shown in Table 1, where each group of defects generally show similar CNR values, except for the shallowest BDH and SDH (marked at locations 4 and 8), which have negative CNR.

In contrast, ECT effectively identified the missing SDH and provided indications for the shallowest BDH and manufactured notch (marked at locations 8 and 14). However, other defects remain undetectable with this modality. Analysis of CNR values reveals that most areas of interest have negative CNR values, even the visible shallowest SDH. This is due to the high variance in signal amplitudes and the similarity in amplitudes between defective and pristine areas. Note that as only a few defects are identifiable in the ECT modality, but CNRs are calculated across all defects present in the inspected sample, the resulting mean and standard deviation values for ECT are negatively biased, reflecting the predominance of undetected defects in the dataset. However, these calculations are retained as they remain important for evaluating improvements observed in the fused datasets over the individual modalities.

Data fusion using the summation method enhances the results in a way that all manufactured defects are visually identifiable from a single dataset. However, this method introduces a large amount of noise, as ECT signal amplitudes in pristine areas are higher than those in PAUT. Therefore, the final fused image exhibits increased amplitudes in these areas, making the interpretation more challenging. As a result, several defects have negative CNRs (marked with 1-4 and 8). Scans and results for the data fusion method for sample A are illustrated in Fig. 8 and Table 1.

The structural noise profile in ECT scans was uneven, particularly around the edges of the ECT scan, due to the imperfect alignment of the padded array with the sample. The ECT probe's soft padding had a limited radius of flexibility, which resulted in horizontal lift-off bands appearing in the final images (Fig. 8b), marking the edge of the inspected sample. This occurrence was unavoidable due to the geometries of the ECT probe and sample surfaces, resulting in different noise levels for individual recorded array channels.

To mitigate this noise, a post-processing channel wise detrending was applied. This is analogous to traditional coil balancing performed during ECT acquisition, where channel-to-channel amplitude offsets caused by lift-off, tilt, or differences in coil sensitivity are minimised [44]. In this case, the baseline for balancing is computed from the recorded scan itself. For each channel x in the ECT array, the channel-wise median across all scan positions is computed:

$$\overline{C}_x = median\left\{C_{ECT}^{norm}(x,y')\right\} \mid y' = 1,..,N \quad \text{Eq. 10}$$

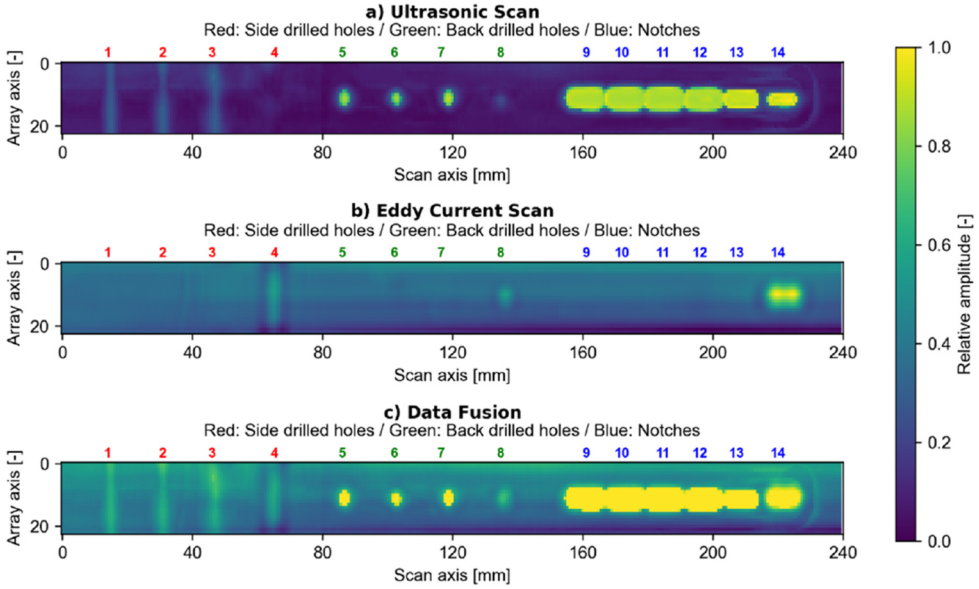


Fig. 8. Results for Sample A with data fusion approach: a) Ultrasonic scan; b) Eddy current scan; c) Data fusion result with side drilled holes (red), back drilled holes (green), and notches (blue) marked. (For interpretation of the references to colour in this figure legend, the reader is referred to the Web version of this article.)

Table 1
Contrast-to-noise ratios for sample A, reported for ultrasound, eddy current, denoised eddy current, data fusion, and denoised data fusion.

Defect ID [−]	Defect type [−]	Depth [mm]	Contrast to Noise Ratio [dB]				
			Ultrasound	Eddy Current	Denoised Eddy Current	Data Fusion	Denoised Fusion
1	SDH	9.5	10.53	−8.62	−4.72	−0.25	6.46
2	SDH	7.5	8.54	−6.79	−4.30	−2.49	5.05
3	SDH	5.5	10.69	−2.29	−4.31	−0.57	10.33
4	SDH	3.5	−12.36	−23.42	−11.85	−3.81	−1.92
5	BDH	8.0	6.59	−15.38	−1.08	5.59	6.44
6	BDH	6.0	4.89	−6.05	−3.13	3.32	5.28
7	BDH	4.0	3.29	−42.90	−1.50	1.91	3.07
8	BDH	2.0	−6.52	8.60	3.44	−21.40	−0.19
9	Notch	12.0	6.46	−9.57	−2.13	5.29	6.28
10	Notch	10.0	9.51	−9.39	−2.42	8.76	9.38
11	Notch	8.0	9.79	−8.93	−2.01	8.97	9.63
12	Notch	6.0	7.96	−5.12	−1.85	6.90	7.79
13	Notch	4.0	18.10	−30.42	−4.16	15.55	17.80
14	Notch	2.0	6.92	7.98	6.97	16.44	21.07
Mean ± St. Dev			6.03 ± 7.22	−10.87 ± 13.30	−2.36 ± 4.06	3.16 ± 8.99	7.60 ± 5.91

The denoised C-scan is then calculated as:

$$C_{ECT}^{denoised}(x,y) = C_{ECT}^{norm}(x,y) - \overline{C}_x \quad \text{Eq. 11}$$

Given that the geometry in the scan direction and the adherence of probes remain relatively constant, the median value effectively captures the amplitude of individual channel noise levels pertinent to lift-off and tilt. This step would significantly reduce the noise bands present in the original scans and accentuate the defective indications, thereby making the final data fusion imaging much clearer and easier to interpret due to the lower amount of noise being translated from ECT scans. It should be noted that not all noise can be removed from ECT scans, and some of it remains visible. This is due to slight ECT probe misalignment, which is almost inevitable during scans, given the challenging geometries and sensitive padded ECT array. Nevertheless, this adjustment positively impacts the CNR values of both the ECT and fused data. For the ECT data, the mean CNR increased by 8.51 dB, while the standard deviation decreased by 9.24 dB. For the fused data, the mean CNR increased by 4.44 dB, and the standard deviation decreased by 3.08 dB. The results, incorporating the noise reduction step in ECT scans, are shown in Fig. 9 and Table 1.

Fig. 10 presents the ROC curves for defect detection using UT, ECT, and the fused C-scan data. The fused modality achieves the highest ROC AUC of 0.918, indicating improved discrimination between defective and non-defective regions compared to either modality alone (0.878 and 0.551 ROC AUC for UT and ECT, respectively). The comparatively lower ROC performance of ECT is attributed to its limited sensitivity to deeper defects present in the sample, resulting in a large proportion of true defect regions being indistinguishable from background noise.

3.2. Results sample B

The PAUT scan of Sample B (Fig. 11a) proved more challenging to scan and interpret, as a more curved geometry resulted in a smaller contact window between the probe and surface. This reduced the beam energy at the corners, leading to the effective capture of only reflections from the centre of the manufactured defects, with the effect being especially noticeable for SDHs. Imperfect probe/surface adherence resulted in noisier scans, especially near the sample's edges, where a more aggressive roll-off was manufactured. Additionally, the effects of the rough machined surface are visible throughout the scan. While all BDHs are visually identifiable, the SDHs exhibit the poorest contrast, with the shallowest ones (13 and 14), located near the sample surface,

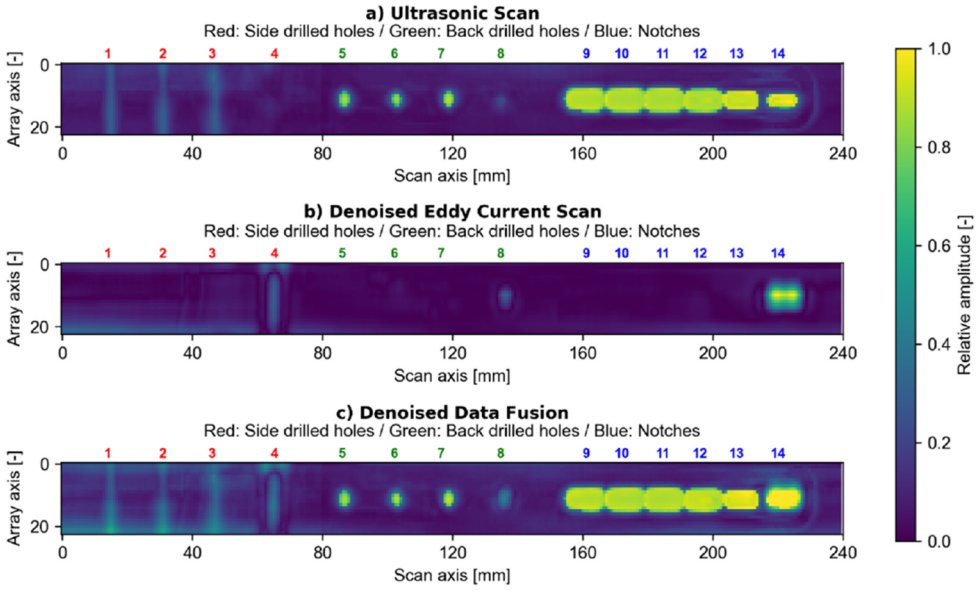


Fig. 9. Results for Sample A with data fusion approach: a) Ultrasonic scan; b) Denoised Eddy current scan; c) Data fusion result with side drilled holes (red), back drilled holes (green), and notches (blue) marked. (For interpretation of the references to colour in this figure legend, the reader is referred to the Web version of this article.)

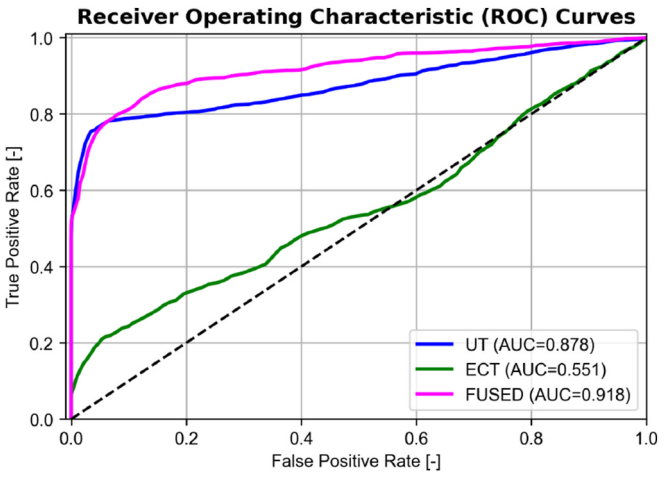


Fig. 10. Sample A: Receiver operating characteristic curves for ultrasonic (blue), eddy current (green), and fused data (pink). (For interpretation of the references to colour in this figure legend, the reader is referred to the Web version of this article.)

being difficult or impossible to discern, as reflected by their negative CNR values.

On the other hand, ECT captured the two SDHs that were missing from the PAUT scan. Additionally, the shallowest BDH (marked with 1) and shallowest offset BDH (marked with 7) are visible in the ECT scans. However, due to the harsher cross-sectional surface profile of the sample, the padded ECT probe's adherence was significantly poorer for this sample, manifesting pronounced horizontal noise bands in the captured ECT signals, which are strongest towards the edges. As a result, the overall CNR is lower compared to the PAUT scan, and in some cases (e.g., defect 7), the CNR becomes negative due to elevated noise variability.

Furthermore, the data fusion approach applied to sample B results in suboptimal clarity, as it introduces even higher levels of noise compared to sample A. The CNR values show that while the centred BDHs (marked 1-6) are distinguishable from the background/noise, other BDHs exhibit negative CNRs despite remaining visually discernible. This is particularly true for the two shallowest SDHs (marked 13 and 14); despite being visible to the naked eye, the high standard deviation in their amplitude values complicates their interpretability.

Applying the same denoising step used in Section 3.1 to minimise the ECT image noise bands in the ECT data of Sample B, also improved both the visual clarity and the CNR values. Specifically, the CNR for defects 1, 7, 13, and 14 (defects captured by the ECT modality) increased. However, the impact of ECT denoising becomes more evident when comparing CNR values for data fusion: the mean CNR increased by 9.02 dB, while the standard deviation decreased by 2.57 dB, resulting in a unified scan in which all defects are clearly visible, aiding data interpretation. Similar to sample A, it was not possible to remove all the noise from the ECT scans due to the slight ECT probe scanning direction misalignment with respect to the sample's length and the complex sample surface geometry. The results with the additional step to remove the noise in ECT scans are presented in Fig. 12 and Table 2.

Fig. 13 presents the ROC curves for defect detection using UT, ECT, and the fused C-scan data of Sample B. Consistent with the observations for Sample A, the fused modality achieves the highest ROC AUC (0.901), compared to UT (0.888) and ECT (0.586).

3.3. Results sample C

The inspection of Sample C represented the most challenging scenario for both PAUT and ECT modalities (Fig. 14a and b) during scanning and data interpretation. For PAUT, the uneven surface profile complicated probe-to-surface coupling, resulting in noisier scans. The observed defect shapes did not precisely match the embedded defects but were overlaid with energy fluctuations caused by the wavy surface. This phenomenon is most evident in the imaging of the longitudinal tungsten insert (highlighted in green in Figs. 14a and 15a) which exhibits a series of discrete high amplitude indications distributed along the inspection direction rather than a continuous monolithic indication. Similar to SDHs from Samples A and B, the transversal tungsten insert is reconstructed as a circular feature (highlighted in orange in Figs. 14a and 15a) since the largest contact area between the sample and the roller probe is close to the centre of the sample. Additionally, at certain locations, due to the position of the roller probe relative to peak/troughs of the WAAM undulated surface, the transmitted acoustic beam deviates from the normal, creating ultrasonic shadows immediately after/before defects, as indicated by magenta rectangles in Figs. 14a and 15a. These

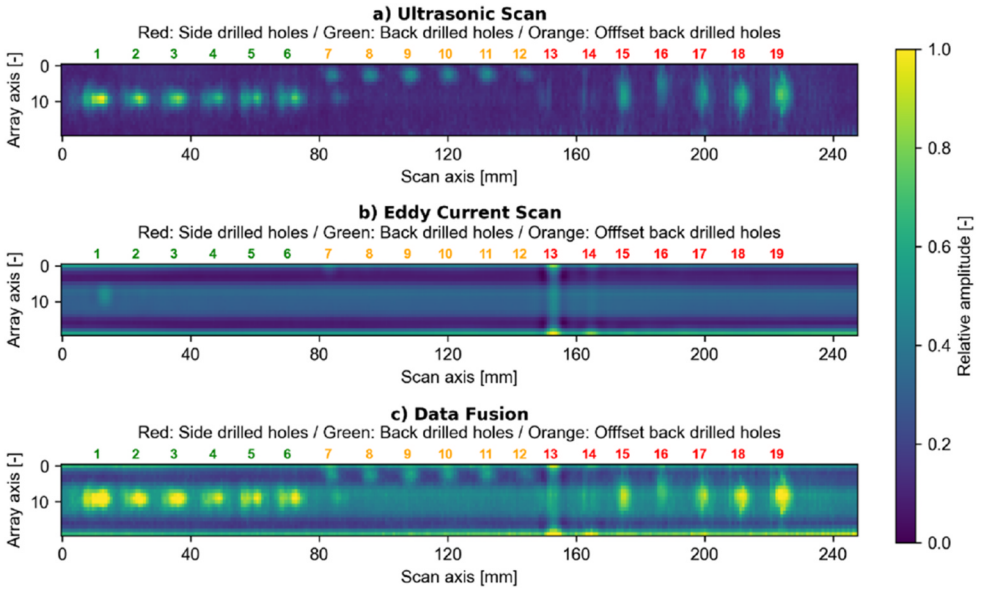


Fig. 11. Results for Sample B with data fusion approach: a) Ultrasonic scan; b) Eddy current scan; c) Data fusion result with side drilled holes (red), back drilled holes (green), and offset back drilled holes (orange) marked. (For interpretation of the references to colour in this figure legend, the reader is referred to the Web version of this article.)

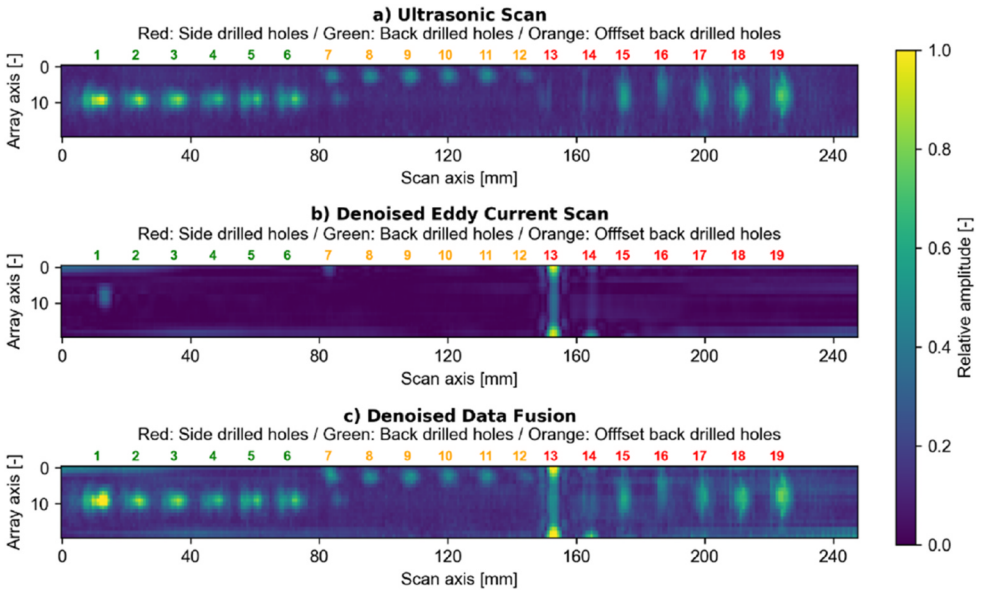


Fig. 12. Results for sample B with data fusion approach: a) Ultrasonic scan; b) Eddy current scan; c) Resulting data fusion approach with side drilled holes (red), back drilled holes (green), and offset back drilled holes (orange) marked. (For interpretation of the references to colour in this figure legend, the reader is referred to the Web version of this article.)

Table 2
Contrast-to-noise ratios for Sample B, reported for ultrasound, eddy current, denoised eddy current, data fusion, and denoised data fusion.

Defect ID [–]	Defect type [–]	Depth [mm]	Contrast to Noise Ratio [dB]				
			Ultrasound	Eddy Current	Denoised Eddy Current	Data Fusion	Denoised Fusion
1	BDH	1.0	13.57	9.97	11.68	12.72	13.27
2	BDH	2.0	13.17	−3.98	−10.52	11.65	13.44
3	BDH	3.0	11.07	−4.16	−9.43	9.71	10.68
4	BDH	4.0	12.31	−5.65	−19.14	8.48	11.77
5	BDH	5.0	16.08	−6.46	−43.20	9.85	15.81
6	BDH	6.0	12.29	−3.26	−5.53	9.36	12.01
7	Offset BDH	1.0	12.88	−19.37	9.84	−2.70	12.67
8	Offset BDH	2.0	17.24	−6.20	−20.22	−1.06	16.72
9	Offset BDH	3.0	14.70	−4.92	−7.59	−0.50	13.94
10	Offset BDH	4.0	12.56	−7.92	−6.56	−3.60	11.89
11	Offset BDH	5.0	13.80	−5.00	−6.11	−1.53	13.20
12	Offset BDH	6.0	11.13	−3.32	−26.41	−8.54	10.29
13	SDH	1.0	−7.05	−0.88	5.98	−0.94	6.86
14	SDH	1.0	−6.29	−19.40	1.22	−12.3	2.18
15	SDH	2.0	3.08	−10.86	−8.11	−3.53	4.56
16	SDH	3.0	2.20	−11.13	−8.82	−4.63	3.88
17	SDH	4.0	3.09	−9.87	−10.54	−4.14	4.23
18	SDH	5.0	1.95	−9.55	−7.59	−3.50	3.45
19	SDH	6.0	3.19	−10.37	−5.44	−0.47	4.85
Mean ± St. Dev			8.47 ± 7.09	−6.97 ± 6.27	−8.76 ± 12.27	0.75 ± 7.07	9.77 ± 4.50

combined effects increase the difficulty of interpretation, making it challenging to distinguish between genuine defect indications and false positives. The resulting CNRs from the PAUT confirm the challenging nature of sample C, with a mean CNR of 3.39 dB being much lower than those of Samples A and B (10.53 dB and 8.47 dB, respectively).

ECT scans of Sample C were performed at two build stages: after layer 4 (following the embedding of tubes) and after layer 5 (following the embedding of tungsten balls). The final ECT dataset used for fusion was a combined image constructed from these two scans, retaining information from both stages. ECT successfully captured four embedded defects, except the 1.0 mm tungsten ball, which was excluded from further analysis. The challenging surface profile and limited flexibility of the ECT array-padded probe made adherence to the sample's surface difficult, resulting in increased noise levels compared to Samples A and B, particularly around the corner radii. This increased noise levels gave rise to challenges in the data interpretation as defective indications were close in the amplitudes compared to background noise, resulting in mean and standard deviation CNR values of -0.03 ± 1.49 dB. This had a negative impact on the data fusion approach, as the added ECT noise easily saturated and overpowers useful signals, with resulting CNR of 2.73 ± 2.00 dB. The results of the PAUT and ECT scan for sample C, alongside data fusion results, are shown in Fig. 14.

Application of the denoising step for ECT provides much clearer imaging of the tungsten balls and the longitudinal insert, with well-defined shapes (Fig. 15b). This improvement is reflected in an increase in the mean CNR value of 3.15 dB; however, the standard deviation of 3.03 dB indicates that noise levels remain elevated compared to Samples A and B, due to the complex surface profile. While transversal SDH defects in Samples A and B were captured fully, the increased curvature in Sample C made the imaging of the transversal tungsten insert less clear, with only its edges captured since the impedance of the coils/channels at these corners is more intensely influenced by the tungsten

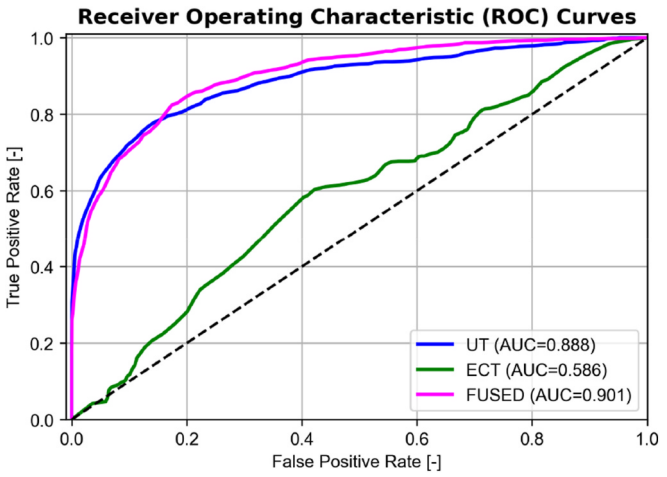


Fig. 13. Sample B: Receiver operating characteristic curves for ultrasonic (blue), eddy current (green), and fused data (pink). (For interpretation of the references to colour in this figure legend, the reader is referred to the Web version of this article.)

tube's conductivity, given the titanium's thinning at corners (highlighted in orange in Figs. 14b and 15b). This specific defect provides an ideal example for the proposed data fusion methodology, where combining UT and ECT images allows the entire defect to be imaged correctly, improving the mean CNR from −1.80 dB (UT) and −2.03 dB (ECT) to 1.45 dB for the fused data. An added benefit of the denoising approach is the clearer separation between true defect indications and acoustic shadows (marked with magenta rectangles in Figs. 14c and 15c). In this case, the shadows are not erroneously amplified by underlying ECT noise, allowing for better visual distinction. This is particularly evident for the 2.0 mm tungsten insert (highlighted in red in Figs. 14c and 15c), where the ECT addition reinforces the correct UT signal, while the neighbouring acoustic shadow remains at a much lower amplitude. Overall, the results for Sample C, shown in Table 3 and Fig. 15, demonstrate CNR improvements with the data fusion approach of 6.03 ± 3.11 dB. While this CNR improvement is more modest compared to Samples A and B (7.60 ± 5.91 dB and 9.77 ± 4.50 dB, respectively), it highlights the potential of the proposed system for in-process implementation.

Similar to previous samples, Fig. 16 presents the ROC curves for defect detection using UT, ECT, and the fused dataset for sample C. The fused dataset again achieves the highest ROC AUC (0.945), followed by UT (0.883) and ECT (0.875). In contrast to Samples A and B, ECT performance is substantially higher in this case, as ECT inspections were conducted after deposition of both layer 4 and layer 5, whereas only a single ECT scan was performed for Samples A and B. The use of multiple ECT inspections increases the likelihood of capturing defects that may not be clearly observable in an individual scan. Nevertheless, the ROC analysis again demonstrates that data fusion provides improved defect detection performance compared to either modality used independently.

In this study, the defect regions used for CNR calculations were defined using prior knowledge of their locations. However, precisely separating the defect boundaries on the scans is challenging, and some surrounding areas may be included unintentionally, making the calculated CNR values sensitive to those choices. However, by keeping the regions consistent across scans, CNR can still provide a useful comparative measure. It should be noted that CNR is not a perfect metric for evaluating image clarity, and deciding if defect visibility is improved is to some extent subjective. While comparing signal-to-noise ratios might seem like a more objective alternative, the different signal characteristics of UT and ECT, especially after fusion, make such comparisons problematic. Therefore, CNR should be interpreted as a relative measure of defect detectability in the presented scenarios.

In a similar manner, the ROC analysis presented in this work relies on manually defined ground truth masks to differentiate defective and pristine regions. Due to the inherently diffuse nature of defect indications in both UT and ECT C-scans, the precise definition of defect boundaries is challenging, and the resulting ground truth definition involves a degree of subjectivity. While this limits the use of ROC analysis as an absolute measure of detection performance, the ground truth definitions were applied consistently within each modality, allowing relative comparisons to be made.

4. Conclusion

In this paper, a data fusion approach between UT and ECT was explored. A study was conducted on two reference titanium components

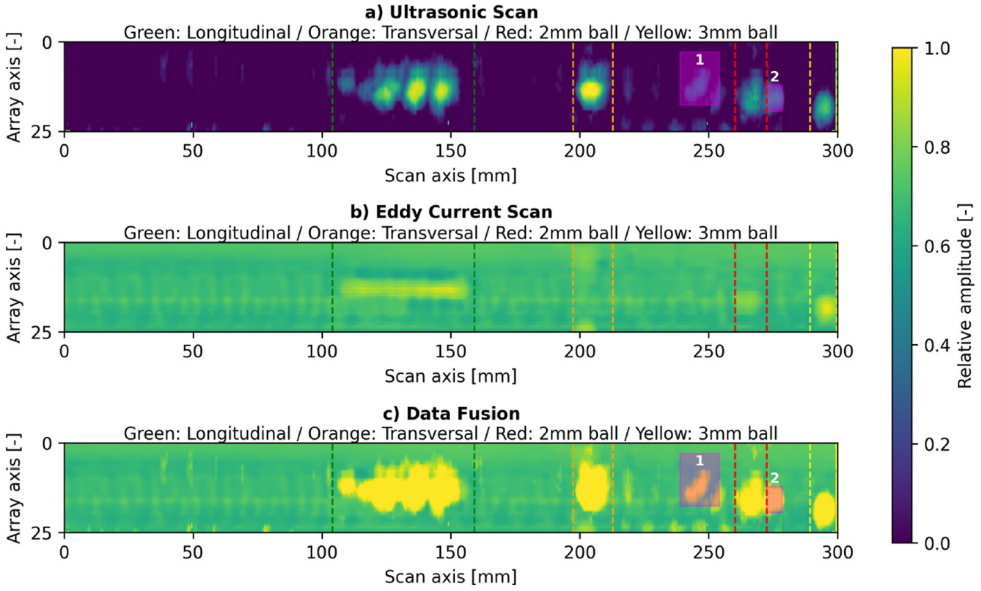


Fig. 14. Results for Sample C with data fusion approach: a) Ultrasonic scan; b) Eddy current scan; c) Data fusion result with longitudinal tungsten insert (green), transversal tungsten insert (orange), 2.0 mm tungsten ball (red) and 3.0 mm tungsten ball (yellow). Rectangles indicated with magenta show ultrasonic shadows. (For interpretation of the references to colour in this figure legend, the reader is referred to the Web version of this article.)

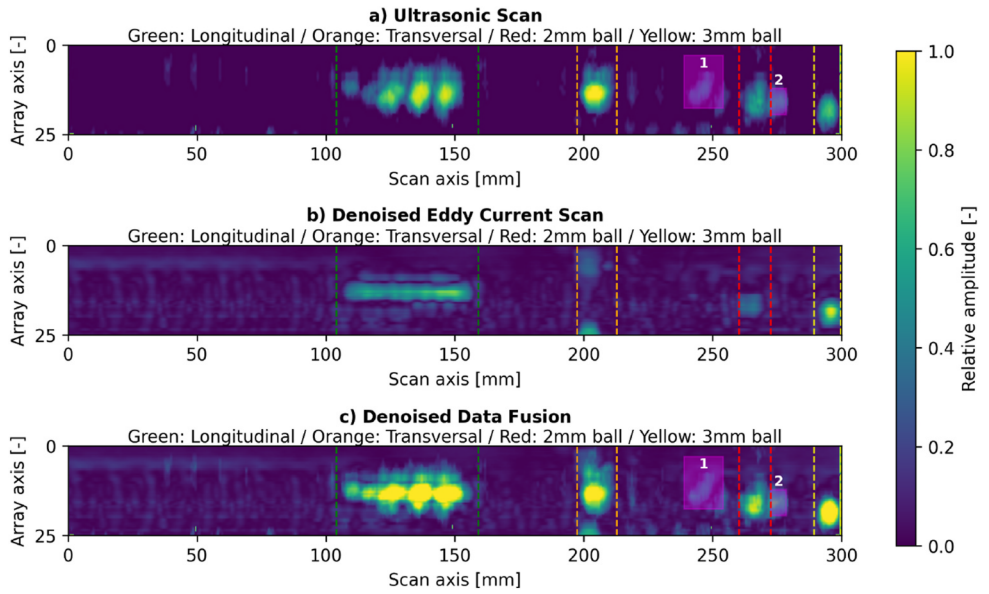


Fig. 15. Results for Sample C with data fusion approach: a) Ultrasonic scan; b) Eddy current scan; c) Data fusion result with longitudinal tungsten insert (green), transversal tungsten insert (orange), 2.0 mm tungsten ball (red) and 3.0 mm tungsten ball (yellow). Rectangles indicated with magenta show ultrasonic shadows. (For interpretation of the references to colour in this figure legend, the reader is referred to the Web version of this article.)

Table 3
Contrast-to-noise ratios for Sample C, reported for ultrasound, eddy current, denoised eddy current, data fusion, and denoised data fusion.

Defect ID [−]	Defect type [−]	Depth from final layer [mm]	Contrast to Noise Ratio [dB]				
			Ultrasound	Eddy Current	Denoised Eddy Current	Data Fusion	Denoised Fusion
1	Longitudinal Tungsten Insert	10.5 mm	6.16	−0.59	4.24	6.11	9.15
2	Transversal Tungsten Insert	10.5 mm	−1.80	1.00	−2.03	1.32	1.45
3	2.0 mm Tungsten Ball	7.0 mm	6.56	−2.18	4.75	2.28	4.92
4	3.0 mm Tungsten Ball	7.0 mm	2.63	1.65	5.63	1.20	8.61
Mean ± St. Dev			3.39 ± 3.37	−0.03 ± 1.49	3.15 ± 3.03	2.73 ± 2.00	6.03 ± 3.11

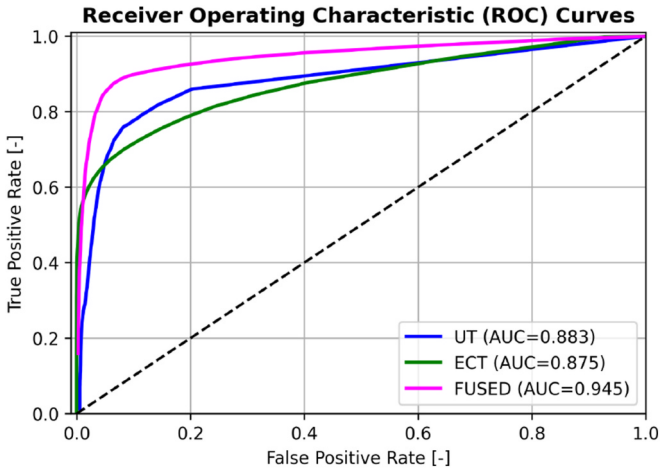


Fig. 16. Sample C: Receiver operating characteristic curves for ultrasonic (blue), eddy current (green), and fused data (pink). (For interpretation of the references to colour in this figure legend, the reader is referred to the Web version of this article.)

containing 33 manufactured defects, and on one WAAM component containing 4 embedded defects. These samples were inspected using an industrial manipulator and a combination of PAUT and ECT arrays mounted on a bespoke design probe bracket, which enabled simultaneous scanning. The study contributions are:

- The development of a closed automation feedback loop consisting of the industrial manipulator, adaptive FT control, and data acquisition from both sensors based on the dual probe bracket design.
- Across all three tested samples, the proposed data fusion approach with ECT denoising improved the CNR. For Sample A, the mean CNR increased from 3.16 ± 8.99 dB to 7.60 ± 5.91 dB, representing a gain of 4.44 dB and a reduction in deviation of 3.08 dB. For Sample B, the CNR improved from 0.75 ± 7.07 dB to 9.77 ± 4.50 dB, corresponding to a gain of 9.02 dB and a deviation reduction of 2.57 dB. Sample C, which presented the most challenging inspection scenario, also benefited from the approach, with the CNR improving from 2.73 ± 2.00 dB to 6.03 ± 3.11 dB. These results confirm that the combination of data fusion and targeted ECT denoising can improve defect visibility compared to raw results, even in more complex WAAM inspection conditions.
- Across all three samples, fused C-scan data consistently achieved higher ROC AUC values compared to individual UT or ECT scans, confirming improved distinction between defective and non-defective regions. For Sample A, fused data achieved an AUC of 0.918, compared to 0.878 for UT and 0.551 for ECT. Sample B showed a similar trend, with fused data resulting in an AUC of 0.901, UT 0.888, and ECT 0.586. Sample C, the most challenging scenario, yielded an AUC of 0.945 for fused data, 0.883 for UT data, and 0.875 for ECT data. These results demonstrate that the proposed data fusion approach improves defect discrimination across varying WAAM inspection conditions.

The limitations of this work include inspecting only straight samples, while WAAM components often feature curved geometries and bends.

Such inspection scenarios pose additional challenges, particularly for ensuring proper sensor delivery. The current dual-probe assembly is suitable for parts with no/low curvature, but sharp bends would require modifications, such as introduction of hinges between the two sensing modalities to maintain consistent sensor contact as the primary axis of each array needs to be normal to the main WAAM profile for best inspection results. Another limitation was the presence of noise in the ECT scans due to alignment imperfections, which slightly affected the presented results. The defects analysed in this study were artificially manufactured, as no readily available datasets of naturally occurring defects in WAAM components exist. The proposed methods are expected to translate well to defects detectable by both NDE modalities, including shallow (i.e., within the effective ECT skin depth) lack of fusion defects, keyholes, and pores that are resolvable by ultrasonic testing and exhibit high acoustic impedance mismatch. In this work, cylindrical and spherical tungsten inclusions were embedded in sample C to approximate the morphology of common WAAM defect types. It should be noted that tungsten has very different electrical conductivity and acoustic properties compared with air. Consequently, for real defects, higher UT signal amplitudes due to the greater Ti/air acoustic impedance mismatch, and lower ECT signal amplitudes because air is non-conductive are expected. Future work will focus on adapting the dual probe assembly and robotic setup for curved WAAM parts, improving ECT sensor positioning, and testing on samples with naturally occurring defects and more challenging surface conditions to better reflect realistic inspection scenarios.

CRediT authorship contribution statement

Vedran Tunukovic: Writing – original draft, Visualization, Software, Methodology, Investigation, Data curation, Conceptualization. **Rylan Gomes:** Writing – review & editing, Data curation. **Shaun McKnight:** Writing – review & editing, Software, Methodology, Investigation, Data curation. **Rastislav Zimermann:** Writing – review & editing, Methodology, Data curation. **Euan Foster:** Writing – review & editing, Data curation. **Charalampos Loukas:** Writing – review & editing, Software, Data curation. **Randika K.W. Vithanage:** Writing – review & editing, Supervision, Resources, Formal analysis. **Ehsan Mohseni:** Writing – review & editing, Validation, Supervision, Resources, Project administration, Funding acquisition, Formal analysis, Conceptualization. **S. Gareth Pierce:** Writing – review & editing, Supervision, Resources, Funding acquisition, Formal analysis. **Charles N. MacLeod:** Writing – review & editing, Resources, Funding acquisition, Formal analysis. **Stewart Williams:** Writing – review & editing, Funding acquisition.

Declaration of competing interest

The authors declare the following financial interests/personal relationships which may be considered as potential competing interests: Ehsan Mohseni reports financial support was provided by RCNDE - UK Research Center in NDE. If there are other authors, they declare that they have no known competing financial interests or personal relationships that could have appeared to influence the work reported in this paper.

Acknowledgements

This work was supported through the Research Centre in Nondestructive Evaluation (RCNDE) Feasibility/Tech Transfer grant.

Data availability

The authors do not have permission to share data.

References

[1] Schröder M, Falk B, Schmitt R. Evaluation of cost structures of additive manufacturing processes using a new business model. Proced CIRP 2015;30:311–6. https://doi.org/10.1016/j.procir.2015.02.144.
[2] Additive manufacturing market size, trend [2025-2033]. https://www.businessresearchinsights.com/market-reports/additive-manufacturing-market-119206?utm_source=chatgpt.com. [Accessed 19 September 2025].
[3] Bhatt PM, Malhan RK, Shembekar AV, Yoon YJ, Gupta SK. Expanding capabilities of additive manufacturing through use of robotics technologies: a survey. Addit Manuf Jan. 2020;31:100933. https://doi.org/10.1016/j.addma.2019.100933.
[4] Zimermann R, et al. In-process non-destructive evaluation of metal additive manufactured components at build using ultrasound and eddy-current approaches. J Manuf Process Dec. 2023;107:549–58. https://doi.org/10.1016/j.jmapro.2023.10.063.
[5] Thapliyal S. Challenges associated with the wire arc additive manufacturing (WAAM) of aluminum alloys. Mater Res Express Oct. 2019;6(11):112006. https://doi.org/10.1088/2053-1591/ab4dd4.
[6] Shaloo M, Schnall M, Klein T, Huber N, Reitinger B. A review of non-destructive testing (NDT) techniques for defect detection: application to fusion welding and future wire arc additive manufacturing processes. Mater 2022;15(10):3697. https://doi.org/10.3390/MA15103697. 15, , pp. 3697–3697, May 2022.
[7] Lu QY, Wong CH. Additive manufacturing process monitoring and control by non-destructive testing techniques: challenges and in-process monitoring. Virtual Phys Prototyp Apr. 2018;13(2):39–48. https://doi.org/10.1080/17452759.2017.1351201.
[8] Pandey A, Gaur V. Effect of dwell time on fatigue properties of wire-arc additively manufactured IN718 alloy. Int J Fatig Nov. 2023;176:107863. https://doi.org/10.1016/j.ijfatigue.2023.107863.
[9] Wooh SC, Shi Y. Optimum beam steering of linear phased arrays. Wave Motion 1999;29(3):245–65. https://doi.org/10.1016/S0165-2125(98)00039-0.
[10] Holmes C, Drinkwater BW, Wilcox PD. Post-processing of the full matrix of ultrasonic transmit–receive array data for non-destructive evaluation. NDT E Int Dec. 2005;38(8):701–11. https://doi.org/10.1016/J.NDTEINT.2005.04.002.
[11] Wilcox PD. Ultrasonic arrays in NDE: beyond the B-scan. In: AIP conf. Proc., 1511; Jan. 2013. https://doi.org/10.1063/1.4789029. 1, pp. 33–33.
[12] Jolly M, et al. Review of non-destructive testing (NDT) techniques and their applicability to thick walled composites. Proced CIRP 2015;38:129–36. https://doi.org/10.1016/J.PROCIR.2015.07.043.
[13] Kim J, Ju SH, Nam J, Kuttolamadom M, Lee C. Non-destructive surface and subsurface characterization of the machined parts by using fiber optic eddy current sensor. J Manuf Process Jun. 2023;95:492–6. https://doi.org/10.1016/j.jmapro.2023.04.039.
[14] Kobayashi N, et al. Fundamental experiments of eddy current testing for additive manufacturing metallic material toward in-process inspection. AIP Conf Proc May 2019;2102(1):070003. https://doi.org/10.1063/1.5099803.
[15] Todorov E, Boulware P, Gaah K. Demonstration of array eddy current technology for real-time monitoring of laser powder bed fusion additive manufacturing process. In: Nondestructive characterization and monitoring of advanced materials, aerospace. SPIE; Mar. 2018. p. 190–201. https://doi.org/10.1117/12.2297511. *Civil Infrastructure, and Transportation XII*.
[16] Mineo C, et al. Flexible integration of robotics, ultrasonics and metrology for the inspection of aerospace components. AIP Conf Proc Feb. 2017;1806(1). https://doi.org/10.1063/1.4974567. 020026–020026.
[17] Mineo C. Automated NDT inspection for large and complex geometries of composite materials. 2015. https://doi.org/10.48730/GXQ8-WA04.
[18] Vasilev M, et al. Sensor-enabled multi-robot system for automated welding and In-Process ultrasonic NDE. Sens 2021;21(15):5077. https://doi.org/10.3390/S21155077. 21, pp. 5077–5077, Jul. 2021.
[19] Duernberger E, MacLeod C, Lines D, Loukas C, Vasilev M. Adaptive optimisation of multi-aperture ultrasonic phased array imaging for increased inspection speeds of wind turbine blade composite panels. NDT E Int Dec. 2022;132:102725. https://doi.org/10.1016/j.ndteint.2022.102725.
[20] Zimermann R, et al. Collaborative robotic wire + arc additive manufacture and sensor-enabled In-Process ultrasonic non-destructive evaluation. Sens 2022;22(11):4203. https://doi.org/10.3390/S22114203. 22, pp. 4203–4203, May 2022.
[21] Javadi Y, et al. In-process inspection of multi-pass robotic welding. Rev Prog Quant Nondestr Eval Dec. 2019;(0) [Online]. Available: https://www.iastatedigitalpress.com/qnde/article/id/8659/.
[22] Javadi Y, et al. In-process calibration of a non-destructive testing system used for in-process inspection of multi-pass welding. Mater Des Oct. 2020;195:108981. https://doi.org/10.1016/j.matdes.2020.108981.
[23] Javadi Y, et al. Continuous monitoring of an intentionally-manufactured crack using an automated welding and in-process inspection system. Mater Des Jun. 2020;191:108655. https://doi.org/10.1016/j.matdes.2020.108655.
[24] Vithanage RKW, et al. A phased array ultrasound roller probe for automated in-Process/Interpass inspection of multipass welds. IEEE Trans Ind Electron Dec. 2021;68(12):12781–90. https://doi.org/10.1109/TIE.2020.3042112.
[25] Vithanage RKW, et al. Development of a phased array ultrasound roller probe for inspection of wire + arc additive manufactured components. J Manuf Process Aug. 2022;80:765–74. https://doi.org/10.1016/j.jmapro.2022.06.045.
[26] Gros XE, Bousigue J, Takahashi K. NDT data fusion at pixel level. NDT E Int 1999;32(5):283–92. https://doi.org/10.1016/S0963-8695(98)00056-5.
[27] Tian GY, Sophian A, Taylor D, Rudlin J. Multiple sensors on pulsed eddy-current detection for 3-D subsurface crack assessment. IEEE Sens J Feb. 2005;5(1):90–6. https://doi.org/10.1109/JSEN.2004.839129.

[28] Mohammad-Djafari A. Fusion of X-ray and geometrical data in computed tomography for nondestructive testing applications. In: Proc. 5th int. Conf. Inf. Fusion FUSION. 1; 2002. p. 309–16. https://doi.org/10.1109/ICIF.2002.1021167. 2002.
[29] Gros XE, Liu Z, Tsukada K, Hanasaki K. Experimenting with pixel-level NDT data fusion techniques. IEEE Trans Instrum Meas Oct. 2000;49(5):1083–90. https://doi.org/10.1109/19.872934.
[30] Simone G, Morabito FC. NDT image fusion using eddy current and ultrasonic data. Int J Comput Math Electr Electron Eng 2001;20(3):332–1649.
[31] J. Yim, S. S. Udpa, L. Udpa, M. Mina, and W. Lord, 'NEURAL NETWORK APPROACHES TO DATA FUSION'.
[32] Song YW, Udpa SS. New morphological algorithm for fusing ultrasonic and eddy current images. Proc IEEE Ultrason Symp 1996;1:649–52. https://doi.org/10.1109/ULTSYM.1996.584059.
[33] Habibalahi A, Safizadeh MS. Pulsed eddy current and ultrasonic data fusion applied to stress measurement. Meas Sci Technol Mar. 2014;25(5):055601. https://doi.org/10.1088/0957-0233/25/5/055601.
[34] Habibalahi A, Dashtbani Moghari M, Samadian K, Mousavi SS, Safizadeh MS. Improving pulse eddy current and ultrasonic testing stress measurement accuracy using neural network data fusion. IET Sci Meas Technol 2015;9(4):514–21. https://doi.org/10.1049/iet-smt.2014.0211.
[35] Edwards RS, Sophian A, Dixon S, Tian GY. Data fusion for defect characterisation using a dual probe system. Sens Actuators Phys May 2008;144(1):222–8. https://doi.org/10.1016/j.sna.2007.12.020.
[36] Guo W, Gao B, Yun Tian G, Si D. Physic perspective fusion of electromagnetic acoustic transducer and pulsed eddy current testing in non-destructive testing system. Philos Trans R Soc Math Phys Eng Sci Sep. 2020;378(2182):20190608. https://doi.org/10.1098/rsta.2019.0608.
[37] KUKA Robotics. KUKA KR90 R3100 extra HA specification manual [Online]. Available: https://www.kuka.com/-/media/kuka-downloads/imported/8350ff3ca11642998dbdc81dcc2ed44c/0000208694_en.pdf; 2023.
[38] Schunk. SCHUNK force torque sensors manual [Online]. Available: https://schunk.com/us/en/automation-technology/force/torque-sensors/ft/ftn-gamma-si-130-10/p/EPIM_ID-30865; 2023.
[39] MicoPulse 6PA | phased array ultrasonic technology | peak NDT [Online]. Available: https://www.peakndt.com/products/micropulse-6pa/.
[40] Non-destructive testing services and technologies | eddyfi. https://www.eddyfi.com. [Accessed 13 May 2024].
[41] Drai R, Sellidj F, Khelil M, Benchaala A. Elaboration of some signal processing algorithms in ultrasonic techniques: application to materials NDT. Ultrasonics 2000;38:503–7.
[42] Benammar A, Drai R, Guessoum A. Detection of delamination defects in CFRP materials using ultrasonic signal processing. Ultrasonics Dec. 2008;48(8):731–8. https://doi.org/10.1016/j.ultras.2008.04.005.
[43] Rodriguez-Molares A, et al. The generalized contrast-to-noise ratio: a formal definition for lesion detectability. IEEE Trans Ultrason Ferroelectrics Freq Control Apr. 2020;67(4):745–59. https://doi.org/10.1109/TUFFC.2019.2956855.
[44] Gomes RCVV, et al. Assessment of out-of-plane ply waviness in carbon-fibre reinforced plastics: comparing different non-destructive evaluation modalities. NDT E Int May 2026;160:103630. https://doi.org/10.1016/j.ndteint.2026.103630.



https://dspace.org/

Automated robotic system for dual ultrasonic and eddy current array integration and data fusion in wire arc additive manufacturing material inspection

Tunukovic, Vedran; Gomes, Rylan; McKnight, Shaun; Zimermann, Rastislav; Foster, Euan A. ...

2026-05
Elsevier
https://doi.org/10.1016/j.ndteint.2026.103665
Tunukovic V, Gomes R, McKnight S, et al., (2026) Automated robotic system for dual ultrasonic and eddy current array integration and data fusion in wire arc additive manufacturing material inspection. NDT & E International, Volume 160, May 2026, Article number 103665

Downloaded from a DSpace repository. https://dspace.org/